The spontaneous passivation of (CoFeNi) (1-x)/3 Cr x alloys in sulfuric acid

Chenyang Xie, Junsoo Han, Junhui Tang, Fan Sun, Kevin Ogle

The spontaneous passivation of $(CoFeNi)_{(100-x)/3}Cr_x$ alloys in sulfuric acid

Chenyang Xie[1], Junsoo Han[2], Junhui Tang[1], Fan Sun[1], Kevin Ogle[1]

[1] Chimie ParisTech, PSL University, CNRS, Institut de Recherche Chimie Paris (IRCP), F-75005 Paris, France

[2] Sorbonne Université, CNRS, Laboratoire Interfaces et Systèmes Electrochimiques (LISE), F-75005 Paris, France

Abstract

The influence of %Cr on the spontaneous passivation of $(CoFeNi)_{(100-x)/3}Cr_x$ alloys in 0.1 M H_2SO_4 was investigated. During spontaneous passivation, Cr enrichment occurs due to the selective dissolution of the matrix elements. The quantity of Cr enrichment is relatively constant with Cr content while the total quantity of alloy dissolved decreases with increasing Cr content. Oxygen reduction is the main driving force for the oxidation / passivation of the alloy at open circuit. %Cr has little effect on the kinetics of oxygen reduction. Element resolved polarization curves predict spontaneous passivation by comparing the critical dissolution rate with the cathodic current.

Table of Symbols

Symbol	Description	Units
A	Surface area of the sample	cm^2
f	Flow rate of the electrolyte	ml min^{-1}
n_M	Number of electrons exchanged in a reaction	
F	Faraday constant	C mol^{-1}
t	Time	s
h(t)	Residence time distribution (RTD)	
X_M	**Nominal composition of M in alloy**	at. %
φ_M	X_{Cr}/X_M	
C_M	Concentration of element M in solution	mol cm^{-3}
E	**Potential**	**V (SCE)**
E_{ap}	Applied potential	V (SCE)
E_{OC}	Open circuit potential	V (SCE)
E_{pp}	Active-passive transition potential from j_e	V (SCE)
$E_{pp,diss}$	Active-passive transition potential from j_{diss}	V (SCE)
E_{TP}	Transpassive potential	V (SCE)
j_e	**Electrical current density**	A cm^{-2}
j_M	Equivalent elemental dissolution current density	A cm^{-2}
j_{diss}	Sum of elemental dissolution current densities	A cm^{-2}
j_{crit}	Active-passive transition current density from j_e	A cm^{-2}
$j_{crit,diss}$	Active-passive transition current density from j_{diss}	A cm^{-2}
j_{pass}	Passive current density	A cm^{-2}
ν_M	**Dissolution rate of an element M**	**mol s^{-1} cm^{-2}**
ν'_M	Normalized ν_M based to bulk composition relative to element M	mol s^{-1} cm^{-2}
$\nu^*_{Cr/M}$	Hypothetical congruent Cr dissolution rate relative to element M	mol s^{-1} cm^{-2}
$\nu_{diss,max}$	Maximum total dissolution rate	mol s^{-1} cm^{-2}
Q_M	**Accumulative dissolution of element M**	**mol cm^{-2}**
Q_{diss}	Accumulative total dissolution	mol cm^{-2}
$Q_{diss\ -\ 300\ s}$	Accumulative total dissolution during the first 300 second	mol cm^{-2}
$Q_{diss\ (30\%\ inhibition)}$	Accumulative total dissolution amount when the total dissolution reaches 30 % of the maximum value	mol cm^{-2}
$\Theta_{Cr/M}$	**Quantity of total enriched Cr relative to M**	**mol cm^{-2}**
$\dot{\Theta}$	Cr enrichment rate relative to M	mol cm^{-2}

1. Introduction

The corrosion resistance of an alloy in most environments depends on its ability to spontaneously passivate at the corrosion potential. This is especially true for localized forms of corrosion such as occur in acidic, occluded environments during pitting and crevice corrosion. As pointed out by G. Frankel in his seminal review of pitting corrosion [1]: “Pit stability depends upon the maintenance of pit electrolyte composition and pit bottom potential that are at least severe enough to prevent repassivation of the dissolving metal surface at the pit bottom.” Measuring and understanding the kinetics of spontaneous passivation is therefore a key issue to understanding localized corrosion phenomena.

Multi-principal element alloys (MPEAs), and more specifically the high entropy alloys (HEAs) [2, 3, 4], have opened a largely unexplored domain in alloy composition. Despite their excellent mechanical properties, corrosion resistance remains a significant challenge to their eventual application [5, 6, 7]. The problem for the MPEAs family is, as with most passive alloys, understanding how each element interacts with the environment and with each other to form a passive film. The situation for the MPEAs is even more acute than conventional alloys due to the complexity of their composition.

An archetypal example of this problem would be understanding the role of Mn in the Cantor alloy. The Cantor alloy [3], characterized by an equiatomic ratio of CoCrFeNiMn and a single face-centered cubic (FCC) structure, was among the first HEAs to be proposed and has received considerable attention due to its excellent mechanical properties [8, 9]. However, it is also known to exhibit poor corrosion resistance in many environments [10]. Of the five alloying elements, Cr is the major contributor to the corrosion resistance *via* the formation of a Cr enriched passive film [11, 12, 13, 14]. By contrast, Mn has proven detrimental to corrosion performance [15, 16]. Yang *et al.* [17] concluded that in 0.1 M H_2SO_4, Mn suppressed the formation of the passive film by enhancing its chemical dissolution rate. Dworschak *et al.* investigated a library of Cantor composition HEAs and reported that the addition of

Mn triggers the dissolution of relatively stable Fe and Cr-based passive films [18]. Efforts have been made to replace the Mn with other elements including Cu [19], Mo [20, 21, 22, 23], W [24], Ti [25], and Nb [26]; however, this is not straightforward as it often leads to the development of secondary phases with deteriorated mechanical properties. Other compositions have been proposed by adding additional species such as N [27], or by optimizing the composition of the alloy, for example $Ni_{38}Fe_{20}Cr_xMn_{21-0.5\ x}Co_{21-0.5x}$ [28]. Improving the chromium content [29] or using new alloy systems while maintaining chromium, such as AlTiVCr [30], has also been explored.

A key to understanding how different alloying elements function in relation to the formation and barrier properties of the passive film would be to assess their effect on the kinetics of spontaneous passivation. This is difficult to measure directly in the laboratory other than through the variations of the open circuit potential, as for example, for the tribocorrosion of stainless steel in H_2SO_4 [31]. Most of the experimental work on the kinetics of repassivation involve the polarization of the material *via* an external power source. The alloy is polarized to a potential in the passive domain, the passive film is breached by a mechanical force (scratch, break, *etc.*), and the resulting current transient is measured [32, 33, 34, 35, 36, 37, 38]. The faradaic component of the current transient is due to elemental dissolution and/or oxide formation. The electrical current is monitored as a function of time and interpreted as either entirely due to oxide formation [39] or entirely due to selective elemental dissolution [37]. Under these conditions of forced passivation, the repassivation rate may be very rapid with repassivation occurring on the order of microseconds.

In recent work, Li *et al.* [27] used element resolved electrochemistry (atomic spectroelectrochemistry, ASEC) to monitor the kinetics of repassivation at open circuit for a Cantor alloy with and without N, a Ni-Cr-Fe-Ru-Mo-W alloy [40], as well as the Ni-Cr and Ni-Cr-Mo family of alloys [41]. These measurements were achieved directly by monitoring the dissolution rates of the different alloying elements while applying a potentiostatic cycle between a cathodic potential to activate the surface followed by a release to the open circuit potential to monitor repassivation. The elemental

dissolution rates of the alloy components were monitored directly as a function of time and the enrichment of Cr relative to the other alloying elements was determined from a mass balance of the elemental dissolution. Under these conditions, it was found that the rate of repassivation was controlled by the degree of oxygen saturation in the electrolyte. This method has the advantage of not only monitoring the kinetics of spontaneous passivation but also by determining specifically which elements undergo dissolution and which elements are enriched in the passive film. Another research on CoCrFeNi alloy also shows the multi-oxide passive film enriched with Cr(III) oxide and will vary under different pH and potential, pH and exposure duration in 0.1 M NaCl [42]. In this work, we investigate the effect of the most significant passivating element, Cr, on the quaternary alloy with composition of $(CoFeNi)_{(100-x)/3}\,Cr_x$ with $15 < x < 25$. The rather narrow range was chosen to establish a background study for the effect of Cr content consistent with the composition of the nearly equiatomic MPEAs. Future works will focus on the effect of Mn, the element most deleterious for passivation of alloy $(NiCrFeCo)_{(100-x)/3}Mn_x$ ($0 \le x \le 20$), and the possibility of replacing Mn with an element X, in the family $(NiCrFeCo)_{95}X_5$.

2. Materials and methods

The metallurgical characterization and composition of the of $(CoFeNi)_{(100-x)/3}\,Cr_x$ are summarized in **Table 1** with a detailed description in **Section 3.1.** The alloys are denoted based on at. % of Cr, for example, 15 at. % Cr as Cr_{15}. The alloys were prepared from Co (99.95%), Cr (99.95%), Fe (99.95%) and Ni (99.99%) (Goodfellow Inc.) in a Buhler AM500 arc melting furnace (three times remelting). After removing the surface oxides by grinding, the ingots were cold rolled with a reduction rate of ~75 % to 0.5 mm thickness. The sheets were then annealed in vacuum tubular furnace under 2.0×10^{-5} Pa at 1273 K for 1 h with subsequent water quenching for recrystallization and homogenization. The samples were cut to square pieces of ~1.5 cm × 2.5 cm in size, grinding with P600 and P1200 SiC paper in sequence and cleaned in ultrasonic bath with acetone and dried with flowing N_2 gas. A 0.1 M H_2SO_4 electrolyte was prepared using reagent grade 95 % concentrated H_2SO_4 and Type-1 water (18 MΩ cm at 25 ℃).

Alloy	Method	Co / at. %	Fe ...	Ni ...	Cr ...	Phase	Grain size / µm
Cr_0	nominal	***33.3***	***33.3***	***33.3***	***0.0***		
	EDX	33.8	33.5	32.7	-	FCC	>88.6
Cr_{15}	nominal	***28.3***	***28.3***	***28.3***	***15.0***		
	EDX	28.4	28.7	27.9	15.0	FCC	8.7
Cr_{20}	nominal	***26.7***	***26.7***	***26.7***	***20.0***		
	EDX	27.1	26.7	26.3	19.9	FCC	7.3
$Cr_{22.5}$	nominal	***25.8***	***25.8***	***25.8***	***22.5***		
	EDX	26.1	25.9	25.5	22.5	FCC	6.9
$Cr_{23.75}$	nominal	***25.4***	***25.4***	***25.4***	***23.8***		
	EDX	25.7	25.5	25.1	23.7	FCC	6.4
Cr_{25}	nominal	***25.0***	***25.0***	***25.0***	***25.0***		
	EDX	25.4	25.2	24.4	25.0	FCC	6.2

Table 1. Atomic composition and grain size of alloys obtained by energy dispersive X-ray (EDX) and electron backscatter diffraction (EBSD) image analysis, respectively. Grain size measurements adhere to the equivalent circular diameter (ECD) method. The EDX-derived composition closely aligns with the nominal composition (average of at least 9-point measurements randomly selected at the sample surface).

Metallurgic characterization

A Zeiss Supra35 field emission gun scanning electron microscope (FEG-SEM) was operated at 15 kV for quantitative energy dispersive X-ray (EDX) micro-analysis with Bruker XFLASH 6/60 spectroscopy system. Electron backscatter diffraction (EBSD) mapping was conducted on a Zeiss Merlin FEG-SEM operated at 20 kV with a Bruker EBSD camera. For EBSD characterization, the as-quenched samples were electropolished to a mirror-like surface finish by using a solution of 4 % perchloric acid in methanol at 0°C. OIM^{TM} analysis software was employed to process inverse pole figures (IPF) and grain size analysis based on the equivalent circular diameter (ECD) method. X-ray diffraction was done with a PANalytical X'Pert diffractometer, scan from 20° to 100° (2θ) with Cu K_α radiation operating at 45 kV and 40 mA.

Atomic spectroelectrochemistry (ASEC)

The ASEC technique has been described in detail elsewhere [43]. The system consists of an inductively coupled plasma – atomic emission spectrometer (ICP-AES) downstream from an electrochemical flow cell such that the dissolution rate of each individual alloying element is measured independently and simultaneously as a function of time. An Ultima 2C^{TM} spectrometer (Horiba, France) was employed for the online elemental analysis. The wavelength of the atomic spectral line used for the elements and the average detection limits ($C_{3\sigma}$), defined by three times the standard deviation of the background signal divided by the sensitivity factors of each alloying element in 0.1 M H_2SO_4 are listed in **Table 2**.

A specially designed electrochemical flow cell with a three-electrode system was used. The alloy specimen served as the working electrode, platinum foil as the counter electrode and saturated calomel electrode (SCE) as the reference electrode were used for electrochemical measurements. Unless otherwise stated, all the potentials are given relative to SCE. A Gamry Reference 600^{TM} potentiostat was used to perform the electrochemical experiments. Unless otherwise stated, the electrolytes were naturally aerated by bubbling air with an air pump into the solution 30 mins before and during the experiments. Spectroscopic data were recorded at 1 point per second, each point being the integral of the emission intensity over the selected time period.

Wavelength (nm)	**Detection limits**	**Co**	**Cr**	**Fe**	**Ni**
		228.62	**267.72**	**259.94**	**231.60**
f = 1.0 ml min^{-1}	$C_{3\sigma}$ (ppb)	6.4 ± 1.1	5.3 ± 0.9	3.3 ± 0.4	12.5 ± 2.1
	ν_M(eq) (pmol s^{-1})	1.8 ± 0.3	1.7 ± 0.3	1.0 ± 0.1	3.4 ± 0.6
f = 2.7 ml min^{-1}	$C_{3\sigma}$ (ppb)	4.8 ± 0.5	4.3 ± 0.7	3.1 ± 0.8	9.7 ± 1.8
	ν_M(eq) (pmol s^{-1})	4.1 ± 0.5	3.9 ± 4	2.6± 0.5	8.2 ± 1.0

Table 2. Detection limits ($C_{3\sigma}$) for the relevant elements at f = 2.7 and 1.0 ml min^{-1}, defined as three times the standard deviation of the background signal of the electrolyte at the given wavelength.

Detection limits may be expressed as concentration or equivalent dissolution rates (ν_{diss}(eq)) calculated from Eq. 1. The error bars were obtained from the standard deviation over several experiments.

Experimental Protocol

The current – potential – time sequence for the potentiodynamic polarization experiment is illustrated in **Fig. 1a**. A cathodic activation step of an E_{ap} of −0.7 V_{SCE} for 5 mins, following which a linear potential sweep at 0.5 mV s^{-1} from −0.7 V_{SCE} to 1.1 V_{SCE} was applied. The current – potential – time sequence for a spontaneous passivation experiment is shown in **Fig. 1b**. The activation step consisted of an applied potential (E_{ap}) of −0.7 V_{SCE} for 10 mins to activate the surface by removing the passive film, followed by an open circuit period (OCP, E_{OC}) for 30 mins to observe the dissolution behavior. The two steps were repeated three times ending with a cathodic activation (−0.7 V_{SCE} vs. SCE). For the visualization of the polarization curves, the potential was corrected for the uncompensated electrolyte resistance (R_Ω, ohms) by subtracting the i R_Ω value from the applied potential, E = E – i R_Ω, where i is the measured electrical current at a given potential in amperes. R_Ω was estimated to be 55 ± 8 Ω from high frequency impedance data at 10 to 100 kHz based on four different trials.

For the spontaneous passivation experiments, a better time resolution was required so the experiments were conducted at f = 2.7 ml min^{-1}. The potentiodynamic experiments require less time resolution, therefore, f = 1.0 ml min^{-1} was used to obtain a better detection limit. Since the flow rate enters directly into the calculation of the dissolution rates, it was measured for each experiment to an accuracy of 1% or better.

Data treatment

The elemental intensity at specific wavelength λ measured by ICP-AES, I_λ, was converted to concentration of element M, C_M, (in nmol cm^{-3}) using standard ICP-AES calibration methods. The elemental dissolution rates, ν_M (nmol s^{-1} cm^{-2}) were determined as:

$$\nu_M = f C_M / A \qquad 1.$$

where f is the flow rate of the electrochemical flow cell, and A is the exposed surface area of the flow cell. The total dissolution rate can be written as:

$$\nu_{diss} = \Sigma_M \nu_M \quad 2.$$

which may be expressed as an equivalent dissolution current density (j_{diss}) to facilitate comparison with the electrical (j_e) current density as:

$$j_{diss} = F \Sigma_M n_M \nu_M \quad 3.$$

where n_M is the number of electrons exchanged for the dissolution of M, and F is the Faraday constant. The ICP-AES method only detects the total dissolved species and is not sensitive to the oxidation state of the elements. Therefore, n_M values are assumed based on thermodynamic data. The following oxidation states were used in this work Ni(II), Cr(III), Fe(II), Mn(II), and Co(II) [44], [45]. Note that these assumptions do not affect the results for the total elemental dissolution or the Cr enrichment determination which is based solely on the dissolution rates.

The excess dissolution of one element relative to another may be determined by comparing the elemental dissolution transients relative to the bulk composition. In this work, Cr was the element which exhibited significant incongruent dissolution, dissolving in excess during activation and being retained during passivation. The rate of Cr enrichment relative to another element M, $\dot{\Theta}$, is given simply by:

$$\dot{\Theta} = d\Theta_{Cr/M}/dt = \nu^*_{Cr/M} - \nu_{Cr} \quad 4$$

where $\nu^*_{Cr/M}$ is the hypothetical congruent Cr dissolution rate with respect to M, which can be defined:

$$\nu^*_{Cr/M} = \varphi_M \nu_M \quad 5$$

where is the stoichiometric factor defined as $\varphi_M = \frac{X_{Cr}}{X_M}$.

In this work, Fe was chosen as reference element M due to its low signal-to-noise ratio of background signal, as evidenced by the relatively low detection limit as shown in **Table 1**. The total enrichment of Cr relative to M may be estimated as a function of time by the sum of $\dot{\Theta}$ from the beginning of the reaction t_0 to a given time t as:

$$\Theta_{Cr/M}(t) = \int_{t_0}^{t} \dot{\Theta}\ dt \quad 6$$

Residence time distributions (RTD)

As compared to the electrochemical transients, the concentration transients have a lower time resolution due to broadening as the elements released from the sample are retained in the flow cell. The shape of the concentration transient resulting from a delta function of dissolution is referred to as the residence time distribution (RTD) or transfer function of the cell, h(t). This was determined experimentally by applying an approximate delta function (4 mA applied current for 1 s) to a nominally pure Cu working electrode in 1 M HCl Ar bubbled solution [46]. The RTD was determined as:

$$h(t) = C_{Cu} / \int_{t_0}^{t_f} C_{Cu} dt \quad 7$$

where t_f is the time at which C_{Cu} has dropped to essentially zero, approximating the limit of $t \rightarrow \infty$. **Fig. S1** in supplementary materials shows the RTD for the flow cell used in this work at 2.7 and 1.0 ml min^{-1} as used for the spontaneous passivation and the potentiodynamic polarization experiments respectively. The time resolution decreases (*i.e.* the RTD becomes broader) as the flow rate is decreased.

3. Results

3.1 Metallurgical Characterization

Six alloys were prepared with a nominal composition of $(CoFeNi)_{(100-x)/3}Cr_x$ with x varying from 0 (Cr_0) to 25 (Cr_{25}) in atomic percent. The metallurgical information for all alloys is given in **Table 1** including the alloy compositions (EDX), the phase information and grain sizes. The alloy composition measured by EDX was within +/-1 at. % range of the nominal composition. More details about the SEM and EDX characterization of the materials are presented in supplementary materials. The XRD patterns and EBSD inverse pole figures for all alloys (**Fig. 2**) indicate single-phase face-centered cubic (FCC) structures, underscoring the stability of the FCC structure with varying Cr content. In alloy without Cr, the grain size was greater than 88 µm, whereas the remaining alloys have similar grain sizes approximately 10x smaller, with a slight

tendency to decrease further with increasing Cr content (**Table 1**). These results indicate that Cr plays a crucial role in grain refinement. While this effect is well-documented in steels due to Cr carbide formation (a), its role in carbon-free MPEAs appears linked to Cr's influence on the growth kinetics of austenite grains. Such grain refinement could also impact mechanical properties according to the Hall-Petch law (b) and potentially affect stress-induced martensitic transformation and mechanical twinning. »

[a] M.A. Razzak, Heat treatment and effects of Cr and Ni in low alloy steel, Bull. Mater. Sci. 34 (2011) 1439–1445. https://doi.org/10.1007/s12034-011-0340-9.
[b] K. Lu, Z. Lei, S. Deng, J. Li, T. Feng, Z. Luo, X. Ma, Synergistic effects of grain sizes on the corrosion behavior and mechanical properties in a metastable high-entropy alloy, Corros. Sci. 225 (2023) 111588. https://doi.org/10.1016/j.corsci.2023.111588.

The IPF maps reveal an FCC structure across all alloy compositions without a preferred grain orientation, indicating homogeneous microstructural characteristics. The surface shows negligible discernible inclusions. Additional SEM images can be found in supplementary materials (**Fig. S2** and **S3**).

3.2 Element resolved polarization curves and Evans diagrams

An overlay of the conventional polarization curves for each alloy in aerated 0.1 M H_2SO_4 is given in **Fig. 3** for a rapid assessment of the electrochemistry of the alloys. The Cr-free alloy (Cr_0) shows the lowest j = 0 potential ($E_{j=0}$) and does not exhibit a passive domain. The Cr containing alloys show a single active to passive transition with a maximum at approximately −0.27 to −0.22 V_{SCE}, followed by a passive domain extending to the onset of transpassive dissolution at approximately 0.85 to 0.90 V_{SCE}. The critical current density (j_{crit}) and passive currents density (j_{pass}) decreased with increasing Cr up to $Cr_{22.5}$ and changed little from $Cr_{22.5}$ to Cr_{25}. j_{crit} was approximately 46 µA cm^{-2} for Cr_{15}, 25 µA cm^{-2} for Cr_{20}, and approximately 18 µA cm^{-2} for the remaining three alloys. j_{pass} varied in a similar manner from 4 µA cm^{-2} for Cr_{15} to 2 µA cm^{-2} for $Cr_{23.75}$. No systematic variation of the transpassive potential (E_{TP}) of 0.9 ± 0.1 V_{SCE} is observed.

Conventional polarization experiments (**Figs. 1b** and **3)** are often used to characterize the tendency of a material to form a passive film. The potential sweep begins in the cathodic domain where the passive film is removed and then reforms as the sweep progresses in the anodic direction. In this way, the kinetics of passive film formation may be reflected by the form and position of the j_e – E characteristic around the zero current potential ($E_{j=0}$). Additional information may be obtained from the element resolved polarization curve as this allows the independent determination of how the rate of the anodic reaction varies with potential.

Results for the six alloys are shown in **Fig. 4** for an anodic scan from –0.7 V_{SCE} to 0.1 V_{SCE}. Shown are the total current density j_e, and the dissolution current density, calculated as the sum of the individual elemental dissolution currents, $j_{diss} = \sum j_M$. The dashed line gives the form of the anodic domain of j_e convoluted with the residence time distribution to add comparison with the dissolution current. The maximum dissolution current density (*i.e.*, $j_{diss,\,crit}$) decreases with increasing %Cr from 46.4 µA cm^{-2} for the Cr_{15}, 36.9 µA cm^{-2} for Cr_{20}, and approximately 6.8 – 10 µA cm^{-2} for the remaining three. Note that these values are in most cases less than the critical current (j_{crit}) measured from the maximum of the anodic active to passive transition of j_e. **Table 3** summarizes the electrochemical parameters determined from the j_e and j_{diss} polarization curves.

A requirement for spontaneous passivation to occur is that the absolute value of the total cathodic current (j_c) at the potential of the dissolution maximum ($E_{pp,diss}$) be larger than the total anodic current necessary for passivation *i.e.*, $abs(j_c(E_{pp,diss})) > j_{diss,crit}$. This situation is often difficult to detect in the conventional polarization curve as j_e represents the sum of the anodic and cathodic currents and the $j_{diss,crit}$ may be buried under the cathodic current.

Alloy	$E_{j=0}$ / V_{SCE}	E_{pp} / V_{SCE}	E^*_{pp} / V_{SCE}	$E_{pp,\,diss}$ / V_{SCE}	j_{crit} / µA cm^{-2}	j^*_{crit} / µA cm^{-2}	$j_{crit,\,diss}$ / µA cm^{-2}
Cr_0	**–0.340**	-	-	-	-	-	-
Cr_{15}	**–0.331**	**–0.271**	**–0.244**	**–0.255**	**58.9**	**54.4**	**46.4**

Cr_{20}	**−0.297**	**−0.253**	**−0.228**	**−0.322**	**26.3**	**23.0**	**36.9**
$Cr_{22.5}$	**−0.276**	**−0.235**	**−0.207**	**−0.263**	**19.0**	**16.6**	**8.5**
$Cr_{23.8}$	**−0.261**	**−0.222**	**−0.196**	**−0.254**	**19.6**	**16.9**	**6.8**
Cr_{25}	**−0.285**	**−0.247**	**−0.220**	**−0.306**	**17.4**	**15.0**	**10.9**

Table 3 Electrochemical parameters obtained from polarization curves in **Fig. 3** and equivalent critical elemental current densities obtained from the ASEC measurements. $E_{pp,diss}$ is the potential where elemental dissolution rates reach a maximum value in active-passive transition domain, and $j_{crit,diss}$ is the equivalent current. E* and j* indicated the values from the convoluted anodic current density curve.

This is illustrated in the diagrams of **Fig. 4**, where the dashed line represents the estimated cathodic current based on a linear Tafel approximation in the cathodic domain extrapolated to beyond the dissolution maximum. The requirement was not met for the Cr_0 and Cr_{15} alloys. The former did not passivate on the time / potential scale of the experiment. For the Cr_{15} alloy the extrapolated Tafel curve intercepted the dissolution peak near the maximum and demonstrated a very slow repassivation kinetics observed for this alloy in **Fig. 6a**. For the remaining alloys with %Cr ≥ 20%, the estimated cathodic current, j_c, is significantly larger than the critical dissolution current and therefore a relatively easy spontaneous passivation is predicted.

Elemental enrichment during the active to passive transition may be observed from the element-resolved polarization curves shown in **Fig. 5,** presenting the elemental dissolution rates (v_M) in the active-passive transition domain of **Fig. 4**. As a reference, the je vs. E curves from **Fig. 3** are shown as dashed curves not to scale on the current axis. For the Cr_0 alloy, the Ni (v_{Ni}) and Fe (v_{Fe}) dissolution rates are essentially identical indicating congruent dissolution. The Co dissolution rate is consistently lower indicating some enrichment of Co which does not appear to inhibit the dissolution rate which increases linearly with applied potential. This could be due to the formation of less soluble Co-based species, such as $CoSO_4$ salt film [47][48]. Sulfates can theoretically be reduced to other species such as sulfides depending on the potential [43], however, the reactions are highly irreversible. Sulfates cannot be

spontaneously reduced in aqueous media near room temperature and are reported to be inert [49].

For the Cr containing alloys, the rate data (ν_{Cr}, < ν_{Co} ≈ ν_{Fe} ≤ ν_{Ni}) indicates that Cr enrichment is coupled with nearly congruent dissolution of Co, Ni, and Fe. Throughout the anodic potential domain of **Fig. 5**, oxide formation is indicated by the observation of $j_e > j_{diss}$. The excess faradaic current could not be accounted for simply by Cr oxidation as the 10 pmol s^{-1} cm^{-2} scale of **Fig. 5** corresponds to 2.9 μA cm^{-2} of Cr oxidation assuming Cr(0) to Cr(III). This would suggest that all the alloying elements contribute to some extent to the oxide film during polarization, at least during the later stages of passivation. Note that the apparent oxide formation occurs after the dissolution maximum. An interpretation of this result is that initially the film is formed only by Cr oxidation products, followed by a period in which the oxidation of the other elements occurs underneath this initial film which blocks their dissolution. This hypothesis will be discussed in a later section.

The element resolved polarization curves presented in this section demonstrate that Cr is the primary element responsible for passivation in this series of alloys: (a) passivation occurred for all Cr containing alloys used in this work which correlated with significant Cr enrichment, and (b) passivation was not observed for the ternary CoFeNi alloy. Further the Evans diagram analysis indicates that the Cr containing alloys should undergo spontaneous passivation, with the exception of Cr_{15} in which the estimated cathodic current at E_{PP} was very close to the $i_{diss,crit}$.

3.2 Spontaneous Passivation at Open Circuit Potential

The tendency of the alloys to spontaneously passivate after cathodic activation is demonstrated in **Fig. 6a** and on an expanded scale for the Cr ≥ 20 at. % alloys in **Fig. 6b**. The OCP (upper) and total dissolution rate, v_{diss}, (lower) profiles for the first activation – OCP cycle are provided. On the potential axis (left) the form of the Cr 20 dissolution transient (Fig. 5) has been added as a dashed curve. This is to serve as a qualitative comparison between the measured OCP and the potentiodynamic elemental dissolution curve.

The results clearly demonstrate the enhanced tendency for spontaneous passivation with increasing Cr content. The Cr_0 showed no spontaneous passivation on the time scale of the experiment: rather there was a continuous dissolution after the release of cathodic potential, stabilizing at about 0.6 nmol cm^{-2} s^{-1} (≈ 0.1 mA cm^{-2}, assuming n_M = 2 for all species). The dissolution rate was decreasing slightly towards the end of the experiment which suggests that passivation might have occurred if the experiment had been conducted for longer times. Likewise, the Cr_0 did not show a significant dissolution peak at the beginning of the activation step; rather it exhibited a continuously decreasing dissolution rate. The Cr_{15} alloy showed an intermediate behavior: During the first ~1000 s, Cr_{15} remained at a steady state with a dissolution rate slightly lower than the Cr_0 at 0.35 nmol cm^{-2} s^{-1} followed by a progressive decrease until the end of the OCP measurement, reaching a rate of approximately 0.15 nmol cm^{-2} s^{-1}. These findings suggest Cr_{15} alloy maintains a relatively weak spontaneous passivation capability in this electrolyte on the time scale of this experiment.

For the alloys with Cr ≥ 20%, a relatively rapid spontaneous passivation is indicated. This is shown more clearly in the expanded scale in **Fig. 6b**. All showed a rapid increase in dissolution rate at t = 0, followed by a peak maximum at 16 – 25 s, and then a decrease to a relatively stable dissolution rate. The dissolution rate peak intensity showed a systematic order of $Cr_{20} > Cr_{22.5} > Cr_{23.75} > Cr_{25}$.

To illustrate qualitatively the relationship between the elemental polarization curve and the tendency towards spontaneous passivation, the form of the elemental polarization curve (on a linear scale, Fig. 5) for Cr_{20} has been overlayed with the potential scale of the OCP transients. The potential of the Cr_0 evolves just to the potential of the Cr_{20} maximum dissolution rate where it remains stable. It does not pass over into the domain where $d\nu_{diss} / dE < 0$. The final potential for the other alloys occurs at a potential more positive than the dissolution rate maximum. The experimental polarization curve is only an approximation of the true steady state curve, and the latter will in any case evolve with time as the alloy surface and

electrolyte evolve. Therefore, this approach is only suggestive but may be useful for the interpretation of the passivation kinetics.

The dashed curve in **Fig. 6b** gives the form of the experimental RTD for the conditions of these experiments. We note that the peak position of the Cr_{25} coincides with the hypothetical RTD trend while the other peaks are shifted to slightly higher times. The Cr_{20} shows an onset consistent with the RTD but is spread out over a longer time.

The quantity of alloy dissolved during spontaneous dissolution decreases with increasing Cr content, %Cr. This is illustrated in **Fig. 7** which presents the total quantity of the dissolved species during 300 s of OCP (spontaneous passivation), $Q_{diss-300\ s}$, as a function of Cr content. Results from the three cycles are numbered according to the cycle (1, 2, and 3). It is seen that the total quantity of alloy dissolved increased from the first cycle to the third cycle, possibly reflecting changes in the near surface alloy composition with continued cycling.

3.3 Elemental Enrichment during Spontaneous Passivation and Activation

Insight into how the surface chemistry changes during passivation and activation may be obtained from the elemental dissolution profiles in **Fig. 8** which compares the rates of all elements during the first 300 s of spontaneous passivation as well as the first 300 s of the following activation (–0.7 V_{SCE} for 1800 – 2100 s). The dissolution rate of Cr was normalized by the bulk composition of Cr, $\nu'_{Cr} = (X_{Fe}/X_{Cr})\nu_{Cr}$ such that $\nu'_{Cr} = \nu_{Fe}$ would imply that the two elements dissolve at a rate proportional to their bulk composition. Ni, Co, and Fe have identical nominal concentrations in the bulk; therefore, normalization was not necessary

During spontaneous passivation, all elemental dissolution rates were above the detection limit. For the Cr containing alloys, the normalized Cr dissolution rate was markedly lower as compared to the other elements by more than a factor of two. This is indicative of the enrichment of Cr during spontaneous passivation. **Fig. 9(a)** shows the enrichment of Cr during the spontaneous passivation cycles determined by **Eq. 6** and **Fig. 9(b)** presents the total quantity of dissolved Cr during the activation cycles, as

a function of %Cr. For the spontaneous passivation step, the estimated quantity of Cr decreases with %Cr, showing a similar trend as the total dissolution. Unlike the total dissolution case, no specific trend with the cycle number is apparent.

The Cr dissolving during the activation step (Q_{Cr}) suggests a nearly constant quantity of approximately 3 nmol cm^{-2}. This would correspond to a uniform film of $Cr(OH)_3$ of ≈ 1 nm assuming the usual bulk density of 2.9 g cm^{-3} [50] if we assume that Fe is not retained in the film during formation. This probably underestimates the film thickness as the film would most likely be hydrated and contain other cations from the alloy. This calculation is much less subject to error than the spontaneous passivation calculation as the measurement is direct, and the assumed bulk composition has no significant influence on the calculation.

4. Discussion

The results indicate that (1) the Cr enrichment occurring during the open circuit exposure, dissolves during the activation step, and (2) the extent of Cr enrichment on the time scale of these experiments does not vary significantly with the %Cr in the alloy over the range of 20 to 25%. However, the quantity of alloy dissolution necessary to obtain this constant Cr enrichment increases markedly as the %Cr is lowered. These results are consistent with the early stages of passivation involving a simple selective dissolution mechanism provided by the overall reaction scheme of Eq. 8 :

$$(CoFeNi)_{(1-x)/3}\,Cr_x\,(s) + 3(x-y)H_2O \rightarrow (x-y)Cr(OH)_3(s) + yCr^{2+} + (1-x)/3\ Fe^{2+}\ (aq) + (1-x)/3\ Ni^{2+}(aq) + (1-x)/3\ [Co^{2+}(aq) + Co^{2+}(s)] + 3(x-y)H^+ + (x-y+2)e^- \quad (8)$$

While this is obviously simplified in that we do not consider other species incorporating into the film, it is consistent with the elemental dissolution results observed here during the early stages of passivation. This mechanism suggests that the amount of alloy dissolution required to produce a constant Cr film content will

be inversely proportional to the %Cr of the alloy. Co may also remain in the film to a lesser extent.

Therefore, we speak of the efficiency by which an alloy will undergo spontaneous passivation in a specific environment as related to the quantity of material dissolved necessary to achieve a certain degree of passivation. In fundamental terms this would be related to the critical dissolution rate coupled with the rate of film nucleation and growth. Practically, this would be an indication of the degree of damage induced by a single depassivation event. This is particularly interesting for the case of spontaneous passivation as the limited time resolution means that the maximum dissolution rate may not be directly measurable.

The concept is elaborated in **Fig. 10** where the relative rate of dissolution ($v_{diss}/v_{diss,max}$) is plotted as a function of the quantity of alloy dissolved (Q_{diss}). The arrows show the point for each alloy where the dissolution rate is reduced to 30% of its maximum. The 30% is arbitrary but in practical terms this would represent a significant decrease in the corrosion rate, and yet the elemental dissolution rates remain readily measurable with good accuracy.

An inverse linear relationship between Q_{diss} (30%) and the at. %Cr of the alloy was found and the value increases with each consecutive cycle. The results follow closely the 300 s dissolution (**Fig. 7**) however, they are reduced by a factor of about 1.5 to 2. The OPC a 30 % inhibition (upper curve, diamonds) was nearly constant at -0.284 V_{SCE} ± 0.004 V with a slight decrease with increasing %Cr. While the results of **Fig. 9** indicate that the Cr enrichment continued until a nearly constant value was obtained, this was not the case for the early stages of passivation. A direct relationship between the Cr enrichment, $\Theta_{Cr/Fe}$(30%) and the Q_{diss} (30%) was observed as shown in **Fig. 11b.** A larger quantity of alloy dissolution and Cr enrichment is necessary to reduce the corrosion rate to 30% for the lower at. % Cr alloys.

The dissolution rate at 30% inhibition also decreases with increasing % Cr since the maximum rate decreases as well. To make this analysis more general, it therefore of interest to characterize the stoichiometric relationship between the dissolution rate, Cr enrichment, and the corrosion potential during spontaneous passivation. The

graphical presentation of **Fig. 12,** shown here for the second cycle of Cr_{20}, is an attempt to represent this in a succent form. **Fig. 12a and b** give the open circuit potential and the dissolution rates of Fe and Cr as a function of time on a linear time scale (**12a**) and time on a log time scale (**12b**). Also shown is the hypothetical congruent Cr dissolution rate, $\nu^*_{Cr/M}$ ($\nu^*_{Cr/M} = \varphi_M \nu_{Fe}$, Eq. 5). The enrichment of Cr is indicated by $\nu_{Cr} < \nu^*_{Cr}$. The rate of Cr enrichment, $\dot{\Theta}$ (Eq. 4), is also shown in **Fig. 12**. The left hand side shows the same rate data plotted as a function of the open circuit potential. The estimated Cr enrichment as a function of time, $\Theta_{Cr/Fe}(t)$ from the integral of $\dot{\Theta}_{Cr}$ (Eq. 6).

Fig. 13 shows the relationship between the dissolution rate, Cr enrichment, and electrochemical potential during spontaneous passivation for the alloys ≥ 20% Cr. The dissolution rate decreased as $\Theta_{Cr}(t)$ increased beyond ≈ 0.4 nmol cm^{-2} as is apparent in **Fig. 12b**. The dissolution peak shows a maximum at −0.304 V_{SCE}. Beyond this point the potential change is slower although the Cr enrichment continues to increase. In the final stages, the dissolution rates of both elements approach the background level and $\dot{\Theta}$ can no longer be distinguished from the background signal. Beyond this point, the measurement of $\dot{\Theta}$ is not reliable. Nevertheless, the potential increased progressively indicating that the passivity was continually enhanced either by thickening of the film or changes in its structure and/or composition. Recall that if congruent oxidation occurs, the film thickening cannot be measured by this method.

Fig. 13 compiles the results for the alloys Cr ≥ 20%. The results of **Fig. 13** indicate that only a small fraction of the total Cr enrichment is necessary to reduce the corrosion rate to a minimal value. However, the Cr enrichment continues to grow with simultaneous increase in the open circuit potential. This period corresponds to the potential range of the polarization curve, **Fig. 4**, where $j_e > j_{diss}$ which supports the idea that the first stage of repassivation involves the formation of an initial Cr rich film, followed by continued oxidation of all elements with minimal dissolution.

The spontaneous passivation event is very different from passivation during a potentiodynamic experiment. In the first case the reaction is driven by oxygen reduction which occurs on the same surface as the formation of the passive film. Under spontaneous conditions the passivation reaction will occur rapidly until partial

passivation is achieved and the oxidizing strength of the electrolyte is no longer able to drive the reaction, at least on the time scale of these experiments. In the second case, the passivation is driven by the power supply with a cathodic reaction on a distant counter electrode. Thus, the passivation reaction will continue well beyond what would normally occur under spontaneous conditions.

Conclusions

This work demonstrates the capacity of the ASEC technique to monitor the rate of spontaneous passivation of a Cr containing alloy and to quantify the enrichment of Cr relative to another element.

During spontaneous passivation, Cr enrichment occurs due to the selective dissolution of the matrix elements. The quantity of Cr enrichment is relatively constant while the total quantity of alloy dissolved decreases with increasing Cr content.

The rate of spontaneous passivation increases slightly with increasing Cr content from 20 to 25%. The quantity of dissolved alloy at the point of a 30% reduction in the maximum dissolution rate during spontaneous passivation, as well as the corresponding Eoc, show a linear decrease with increasing Cr content A significantly slower rate was observed for 15% Cr, and no passivation was observed for 0% Cr.

For this family of alloys (15 - 25 at. % Cr) in 0.1 M H_2SO_4 solution, Cr is the primary element responsible for passivation. In the absence of Cr, spontaneous passivation does not occur.

The Cr containing alloys show a single dissolution peak that in most cases is partially hidden in the polarization curve by the cathodic current. The critical dissolution current, determined as the maximum in the elemental polarization curve, is shifted to

lower potential than the critical current, measured as the maximum in the conventional polarization curve.

Oxygen reduction is the main driving force for the oxidation / passivation of the alloy. The %Cr has little effect on the kinetics of oxygen reduction. The ability of the alloy to spontaneously passivate may be qualitatively deduced from the element resolved polarization curve by comparing the **critical dissolution rate** with the cathodic current at the potential of the maximum dissolution.

The degree of passivation is not linear with the Cr enrichment. The rate falls off very quickly at first and much more slowly at longer times. This demonstrates a major difference between spontaneous passivation driven by oxygen reduction in the electrolyte and potentiodynamic passivation driven by the power supply of a potentiostat.

Acknowledgements

This work was partially supported by the Agence Nationale de Recherche, France, grant #ANR-20-CE08-0031 (Tapas2020 project). Mr. Junhui TANG is sponsored by China Scholarship Council.

CRediT author statement:

Chenyang Xie: Conceptualization, Data curation, Investigation, Methodology, Writing – original draft. **Junsoo Han:** Conceptualization, Writing – review and editing. **Junhui Tang:** Investigation, Resources. **Fan Sun:** Investigation, Resources, Writing – review and editing. **Kevin Ogle:** Conceptualization, Funding acquisition, Methodology, Supervision, Writing – review and editing.

Declaration of Competing Interest:

The authors declare that they have no known competing financial interests or personal relationships that could have appeared to influence the work reported in this paper.

Reference

[1] G.S. Frankel, Pitting Corrosion of Metals: A Review of the Critical Factors, *J. Electrochem. Soc.*, 145 (1998) 2186. https://doi.org/10.1149/1.1838615.

[2] Yeh, J.-W., S.-K. Chen, S.-J. Lin, J.-Y. Gan, T.-S. Chin, T.-T. Shun, C.-H. Tsau, and S.-Y. Chang. "Nanostructured High-Entropy Alloys with Multiple Principal Elements: Novel Alloy Design Concepts and Outcomes." *Advanced Engineering Materials* **6**(2004)299–303. https://doi.org/10.1002/adem.200300567.

[3] Cantor, B., I. T. H. Chang, P. Knight, and A. J. B. Vincent. "Microstructural Development in Equiatomic Multicomponent Alloys." *Materials Science and Engineering: A* **375-377**(2004): 213–18. https://doi.org/10.1016/j.msea.2003.10.257.

[4] T. K. Chen,,- T. T. Shun, J. W. Yeh, M. S. Wong, "Nanostructured Nitride Films of Multi-Element High-Entropy Alloys by Reactive DC Sputtering", *Surface and Coatings Technology*, **188–189**(2004)193–200. https://doi.org/10.1016/j.surfcoat.2004.08.023.

[5] Y. Qiu, S. Thomas, M.A. Gibson, H. L. Fraser, N. Birbilis, "Corrosion of high entropy alloys", *npj Mater Degrad,* **1**(2017)15. https://doi.org/10.1038/s41529-017-0009-y

[6] N. Birbilis, S. Choudhary, J.R. Scully, M.L. Taheri, A perspective on corrosion of multi-principal element alloys, Npj Mater Degrad 5 (2021) 1–8. https://doi.org/10.1038/s41529-021-00163-8.

[7] M. Ghorbani, Z. Li, Y. Qiu, P. Marcus, J.R. Scully, O. Gharbi, H. Luo, R.K. Gupta, Z.R. Zeng, H.L. Fraser, M.L. Taheri, N. Birbilis, "Current progress in corrosion of multi principal element alloys" *arXiv*:2405.05623v1 [cond-mat.mtrl-sci], https://doi.org/10.48550/arXiv.2405.05623

[8] B. Gludovatz, A. Hohenwarter, D. Catoor, E.H. Chang, E.P. George, R.O. Ritchie, A fracture-resistant high-entropy alloy for cryogenic applications, *Science* 345 (2014) 1153–1158. https://doi.org/10.1126/science.1254581.

[9] F. Otto, A. Dlouhý, Ch. Somsen, H. Bei, G. Eggeler, E.P. George, The influences of temperature and microstructure on the tensile properties of a CoCrFeMnNi high-entropy alloy, *Acta Materialia* 61 (2013) 5743–5755. https://doi.org/10.1016/j.actamat.2013.06.018.

[10] H. Luo, Z. Li, A.M. Mingers, D. Raabe, Corrosion behavior of an equiatomic CoCrFeMnNi high-entropy alloy compared with 304 stainless steel in sulfuric acid solution, *Corros. Sci.* 134 (2018) 131–139. https://doi.org/10.1016/j.corsci.2018.02.031.

[11] L. Wang, D. Mercier, S. Zanna, A. Seyeux, M. Laurent-Brocq, L. Perrière, I. Guillot, P. Marcus, Study of the surface oxides and corrosion behaviour of an equiatomic CoCrFeMnNi high entropy alloy by XPS and ToF-SIMS *Corros. Sci.* 167 (2020) 108507. https://doi.org/10.1016/j.corsci.2020.108507.

[12] K.F. Quiambao, S.J. McDonnell, D.K. Schreiber, A.Y. Gerard, K.M. Freedy, P. Lu, J.E. Saal, G.S. Frankel, J.R. Scully, Passivation of a corrosion resistant high entropy alloy in non-oxidizing sulfate solutions, Acta Mater. 164 (2019) 362–376. https://doi.org/10.1016/j.actamat.2018.10.026.

[13] T. Li, O.J. Swanson, G.S. Frankel, A.Y. Gerard, P. Lu, J.E. Saal, J.R. Scully, Localized corrosion behavior of a single-phase non-equimolar high entropy alloy, Electrochimica Acta 306 (2019) 71–84. https://doi.org/10.1016/j.electacta.2019.03.104.

[14] J. Han, A.Y. Gerard, P. Lu, J.E. Saal, K. Ogle, J.R. Scully, Elementally Resolved Dissolution Kinetics of a Ni-Fe-Cr-Mn-Co Multi-Principal Element Alloy in Sulfuric Acid Using AESEC-EIS, J. Electrochem. Soc. 169 (2022) 081507. https://doi.org/10.1149/1945-7111/ac862b.

[15] J. Han, X. Li, A.Y. Gerard, P. Lu, J.E. Saal, G.S. Frankel, K. Ogle, J.R. Scully, Potential Dependent Mn Oxidation and Its Role in Passivation of Ni38Fe20Cr22Mn10Co10 Multi-Principal Element Alloy Using Multi-Element Resolved Atomic Emission Spectroelectrochemistry, J. Electrochem. Soc. 168 (2021) 051508. https://doi.org/10.1149/1945-7111/ac0062.

[16] H. Torbati-Sarraf, M. Shabani, P.D. Jablonski, G.J. Pataky, A. Poursaee, The influence of incorporation of Mn on the pitting corrosion performance of CrFeCoNi High Entropy Alloy at different temperatures, Mater. Des. 184 (2019) 108170. https://doi.org/10.1016/j.matdes.2019.108170.

[17] J. Yang, J. Wu, C.Y. Zhang, S.D. Zhang, B.J. Yang, W. Emori, J.Q. Wang, Effects of Mn on the electrochemical corrosion and passivation behavior of CoFeNiMnCr high-entropy alloy system in H2SO4 solution, *J. Alloys Compd.* 819 (2020) 152943. https://doi.org/10.1016/j.jallcom.2019.152943.

[18] D. Dworschak, K.K. Tseng, J.W. Yeh, H.W. Cheng, M. Valtiner, “Bottom-up characterization of electrochemical passivity from simple binary alloys to high entropy alloys”, *Electrochim. Acta*, 405(2022)139804, https://doi.org/10.1016/j.electacta.2021.139804

[19] Y.-J. Hsu, W.-C. Chiang, J.-K. Wu, Corrosion behavior of FeCoNiCrCux high-entropy alloys in 3.5% sodium chloride solution, *Mater. Chem. Phys.* 92 (2005) 112–117. https://doi.org/10.1016/j.matchemphys.2005.01.001.

[20] X.-L. Shang, Z.-J. Wang, Q.-F. Wu, J.-C. Wang, J.-J. Li, J.-K. Yu, Effect of Mo Addition on Corrosion Behavior of High-Entropy Alloys CoCrFeNiMox in Aqueous Environments, *Acta Metall. Sin. Engl. Lett.* 32 (2019) 41–51. https://doi.org/10.1007/s40195-018-0812-7.

[21] Z. Wang, J. Jin, G.-H. Zhang, X.-H. Fan, L. Zhang, Effect of temperature on the passive film structure and corrosion performance of CoCrFeMoNi high-entropy alloy, *Corros. Sci.* 208 (2022) 110661. https://doi.org/10.1016/j.corsci.2022.110661.

[22] X. Wang, D. Mercier, S. Zanna, A. Seyeux, L. Perriere, M. Laurent-Brocq, I. Guillot, V. Maurice, P. Marcus, Effects of Chloride Ions on Passive Oxide Films Formed on Cr-Fe-Co-Ni(-Mo) Multi-Principal Element Alloy Surfaces, J. Electrochem. Soc. 170 (2023) 041506. https://doi.org/10.1149/1945-7111/accb10.

[23] X. Wang, D. Mercier, S. Zanna, A. Seyeux, L. Perriere, M. Laurent-Brocq, I. Guillot, V. Maurice, P. Marcus, Origin of enhanced passivity of Cr–Fe–Co–Ni–Mo multi-principal element alloy surfaces, Npj Mater. Degrad. 7 (2023) 1–10. https://doi.org/10.1038/s41529-023-00330-z.

[24] C. Shang, E. Axinte, J. Sun, X. Li, P. Li, J. Du, P. Qiao, Y. Wang, CoCrFeNi(W1 − xMox) high-entropy alloy coatings with excellent mechanical properties and corrosion resistance prepared by mechanical alloying and hot pressing sintering, *Mater. Des.* 117 (2017) 193–202. https://doi.org/10.1016/j.matdes.2016.12.076.

[25] E. Heidari, M. Atapour, A. Obeydavi, The effect of Cr-content on the corrosion behavior of Ti0.5Mo0.5CoNiMnCrx high-entropy alloy thin films deposited by direct current magnetron sputtering, J. Alloys Compd. 976 (2024) 173265. https://doi.org/10.1016/j.jallcom.2023.173265.

[26] S. Shuang, Z.Y. Ding, D. Chung, S.Q. Shi, Y. Yang, Corrosion resistant nanostructured eutectic high entropy alloy, *Corros. Sci.* 164 (2020) 108315. https://doi.org/10.1016/j.corsci.2019.108315.

[27] X. Li, P. Zhou, H. Feng, Z. Jiang, H. Li, K. Ogle, Spontaneous passivation of the CoCrFeMnNi high entropy alloy in sulfuric acid solution: The effects of alloyed nitrogen and dissolved oxygen, *Corros. Sci.* 196 (2022) 110016. https://doi.org/10.1016/j.corsci.2021.110016.

[28] A.Y. Gerard, E.J. Kautz, D.K. Schreiber, J. Han, S. McDonnell, K. Ogle, P. Lu, J.E. Saal, G.S. Frankel, J.R. Scully, The role of chromium content in aqueous passivation of a non-equiatomic Ni38Fe20CrxMn21-0.5xCo21-0.5x multi-principal element alloy (x = 22, 14, 10, 6 at%) in acidic chloride solution, *Acta Mater.* 245 (2023) 118607. https://doi.org/10.1016/j.actamat.2022.118607.

[29] G.Y. Koga, N. Birbilis, G. Zepon, C.S. Kiminami, W.J. Botta, M. Kaufman, A. Clarke, F.G. Coury, Corrosion resistant and tough multi-principal element Cr-Co-Ni

alloys, Journal of Alloys and Compounds 884 (2021) 161107. https://doi.org/10.1016/j.jallcom.2021.161107.

[30] S. Choudhary, Y. Qiu, S. Thomas, N. Birbilis, Element-resolved electrochemical analysis of transpassive dissolution and repassivation behavior of the multi-principal element alloy AlTiVCr, Electrochimica Acta 362 (2020) 137104. https://doi.org/10.1016/j.electacta.2020.137104.

[31] P. Henry, J. Takadoum, P. Berçot, "Tribocorrosion of 316L stainless steel and TA6V4 alloy in H_2SO_4 media", *Corr. Sci.*, 51(2009)1308-1314. https://doi.org/10.1016/j.corsci.2009.03.015

[32] J.F. Rimbert, J. Pagetti, Repassivation kinetics studies on an austenitic stainless steel in chloride media, *Corr. Sci.*, 20 (1980) 189–210. https://doi.org/10.1016/0010-938X(80)90131-6.

[33] G.S. Frankel, B.M. Rush, C.V. Jahnes, C.E. Farrell, A.J. Davenport, H.S. Isaacs, Repassivation transients measured with thin film breaking electrodes, *J. Electrochem. Soc.*, 138 (1991) 643–644. https://doi.org/10.1149/1.2085652.

[34] R.G. Kelly, R.C. Newman, Conformation of the applicability of stratched electrode techniques for the determination of bare surface current densities, *J. Electrochem. Soc.*, 137 (1990) 357–358. https://doi.org/10.1149/1.2086427.

[35] R.W. Bosch, B. Schepers, M. Vankeerberghen, Development of a scratch test in an autoclave for the measurement of repassivation kinetics of stainless steel in high temperature high pressure water, *Electrochim. Acta* 49 (2004) 3029–3038. https://doi.org/10.1016/j.electacta.2004.01.062.

[36] H. S. Kwon, E. A. Cho, and K. A. Yeom, "Prediction of Stress Corrosion Cracking Susceptibility of Stainless Steels Based on Repassivation Kinetics", *Corrosion*, **56** (2000)32–40. https://doi.org/10.5006/1.3280519

[37] R.S. Lillard, G. Vasquez, D.F. Bahr, The Kinetics of Anodic Dissolution and Repassivation on Stainless Steel 304L in Solutions Containing Nitrate, *J. Electrochem. Soc.* 158 (2011) C194. https://doi.org/10.1149/1.3574367.

[38] G.T. Burstein, P.I. Marshall, Growth of passivating films on scratched 304L stainless steel in alkaline solution, *Corr. Sci.*, 23 (1983) 125–137. https://doi.org/10.1016/0010-938X(83)90111-7.

[39] G.T. Burstein, P.I. Marshall, The coupled kinetics of film growth and dissolution of stainless steel repassivating in acid solutions, *Corr. Sci.*, 24 (1984) 449–462. https://doi.org/10.1016/0010-938X(84)90070-2.

[40] X. Li, J. Han, P. Lu, J.E. Saal, G.B. Olson, G.S. Frankel, J.R. Scully, K. Ogle, Communication—Dissolution and Passivation of a Ni-Cr-Fe-Ru-Mo-W High Entropy Alloy by Elementally Resolved Electrochemistry, *J. Electrochem. Soc.* 167 (2020) 061505. https://doi.org/10.1149/1945-7111/ab7f86.

[41] X. Li, K. Ogle, The Passivation of Ni-Cr-Mo Alloys: Time Resolved Enrichment and Dissolution of Cr and Mo during Passive-Active Cycles, *J. Electrochem. Soc.* 166 (2019) C3179. https://doi.org/10.1149/2.0201911jes.

[42] S. Choudhary, N. Birbilis, S. Thomas, Evolution of Passivity for the Multi-Principal Element Alloy CoCrFeNi with Potential, pH, and Exposure in Chloride Solution, CORROSION 78 (2022) 49–57. https://doi.org/10.5006/3902.

[43] K. Ogle, Atomic Emission Spectroelectrochemistry: Real-Time Rate Measurements of Dissolution, Corrosion, and Passivation, *Corrosion* **75** (2019) 1398–1419. https://doi.org/10.5006/3336.

[44] M. Pourbaix, Atlas of electrochemical equilibria in aqueous solutions, *National Association of Corrosion Engineers*, Houston, Texas, 1974.

[45] K. Wang, J. Han, A.Y. Gerard, J.R. Scully, B.-C. Zhou, Potential-pH diagrams considering complex oxide solution phases for understanding aqueous corrosion of multi-principal element alloys, Npj Mater. Degrad. 4 (2020) 1–11. https://doi.org/10.1038/s41529-020-00141-6.

[46] V. Shkirskiy, P. Maciel, J. Deconinck, K. Ogle, On The Time Resolution of the Atomic Emission Spectroelectrochemistry Method, J. Electrochem. Soc. 163 (2016) C37–C44. https://doi.org/10.1149/2.0991602jes

[47] I. Epelboin, C. Gabrielli, Ph. Morel, Etude de la passivation du cobalt en milieu sulfurique, Electrochimica Acta 18 (1973) 509–513, https://doi.org/10.1016/0013-4686(73)80056-8.

[48] K.H. Kim, S.H. Lee, N.D. Nam, J.G. Kim, Effect of cobalt on the corrosion resistance of low alloy steel in sulfuric acid solution, Corros. Sci. 53 (2011) 3576–3587. https://doi.org/10.1016/j.corsci.2011.07.001.

[49] G. Charlot, "L'analyse quantitative et les réactions en solution (Masson et Cie, Paris), 4th Ed., p. 298 (1957).

[50] chromium(iii)hydroxide, (n.d.). https://www.chembk.com/en/chem/chromium(iii)hydroxide (accessed June 24, 2024).

Figure Captions

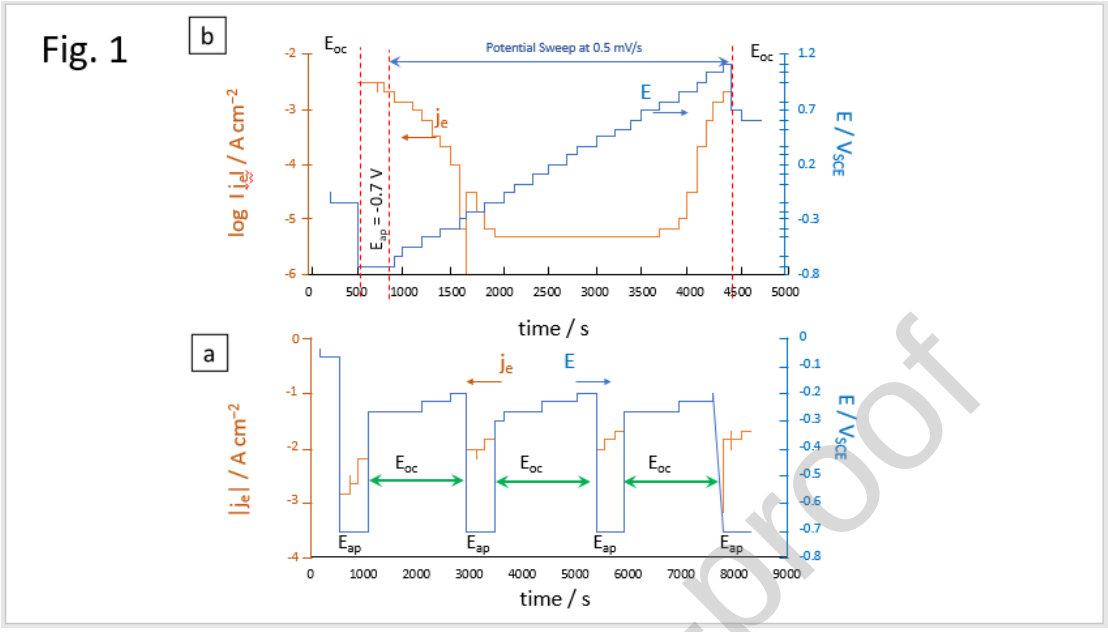

Fig. 1 Two electrochemical sequences used to investigate passivation for Cr_{20} in 0.1 M H_2SO_4. (a) Polarization experiments $E_{OC}(1)$- cathodic hold, potential sweep at 0.5 mV s^{-1}, and $E_{OC}(2)$ at f = 1.0 ml min^{-1}. (b) Spontaneous passivation current – potential – time profile for an active-passive sequence at f = 2.7 ml min^{-1}.

Fig. 2

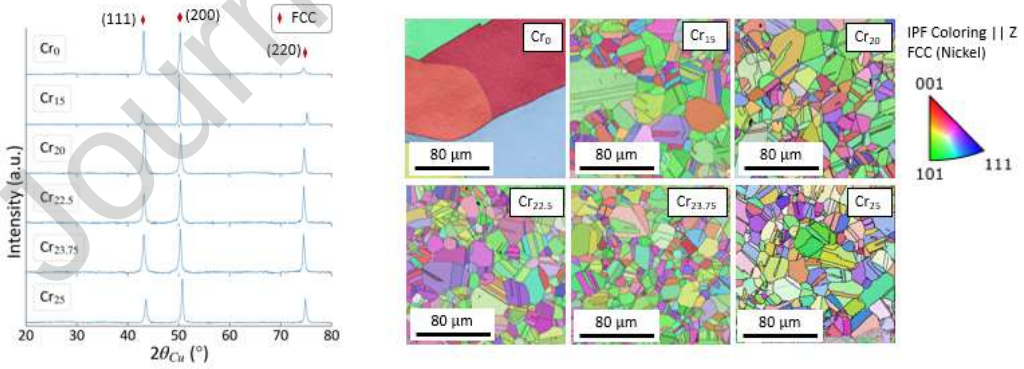

Fig. 2 XRD patterns (left) and inverse pole figure (IPF) maps (right) for $(CoFeNi)_{(100-x)/3}Cr_x$ (x = 0, 20, 22.5, 23.75, 25 at. %) alloys. The spectra confirm the FCC crystal structure for all alloy compositions, with no additional peaks detected, indicating negligible secondary phases or anomalies. Grain size details are provided in **Table 2**.

Fig. 3

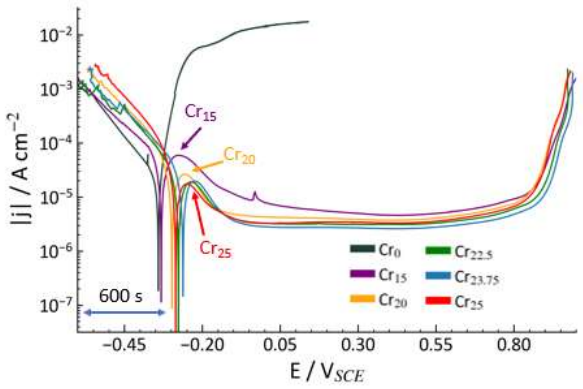

Fig. 3. Polarization curves of $(CoFeNi)_{(100-x)/3}Cr_x$ (x = 0, 20, 22.5, 23.75, 25 at. %) alloy in 0.1 M H_2SO_4 (air saturated, ambient temperature) from −0.7 to 1.1 V_{SCE} with a scan rate of 0.5 mV s^{-1} and a flow rate of 1 ml min^{-1}. E_{ap} (−0.7 V_{SCE}) represents the cathodic potential used for activation. The potential was corrected for the iR_Ω as described in the experimental section. Electrochemical parameters can be found in **Table 3**.

Fig. 4

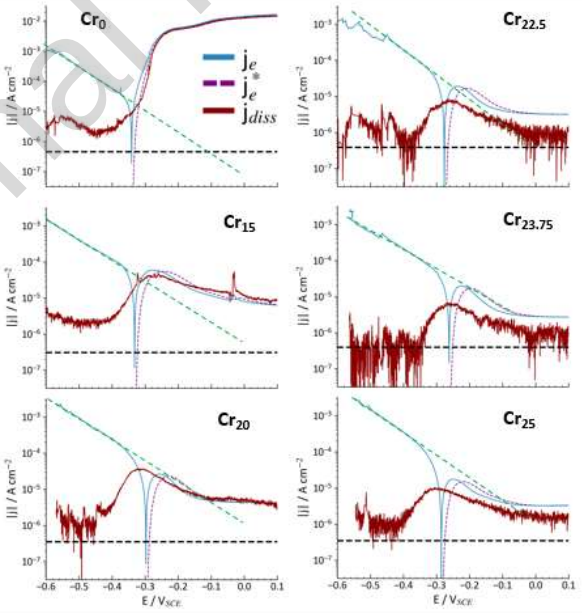

Fig. 4 Experimental Evans diagrams for the six alloys in air bubbled 0.1 M H_2SO_4 showing the electrochemical current density (j_e) and the dissolution current density (j_{diss}). The dashed line in green is an approximate extrapolation of a cathodic Tafel rate law. The dashed horizontal line corresponds to the approximate detection limit under the conditions of the experiment. The j_e curve is identical to that presented in

Fig. 3. The potential was corrected for the iR_Ω as described in the experimental section.

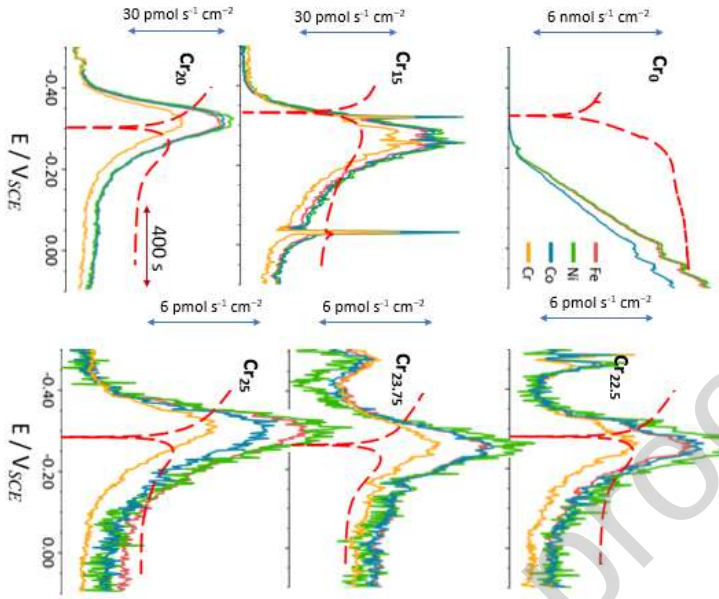

Fig. 5

Fig. 5 Elemental dissolution rates obtained during the polarization curves of **Fig. 4** demonstrating the enrichment of Cr during the active-passive transition and the passive domain. As a reference, the dotted red curve is the form of the j_e vs. E profile from Fig 4, the vertical axis not to scale. Cr has been normalized to the hypothetical congruent Cr dissolution rate (nominal bulk composition), such that the difference between the Cr and the Fe reflects the surface enrichment. Note that Cr_{15} and Cr_{20} are on an identical equivalent current scale (30 pmol s^{-1} cm^{-2}). $Cr_{22.5}$, $Cr_{23.75}$, and Cr_{25} are an identical magnified scale, and Cr_0 is on a (6 nmol s^{-1} cm^{-2} scale). The dark arrows indicate the $E_{j=0}$ from **Fig. 3**. A boxcar averaging (N = 5) was used for the ASEC results to improve the signal-to-noise ratio. The potential was corrected for the iR_Ω as described in the experimental section.

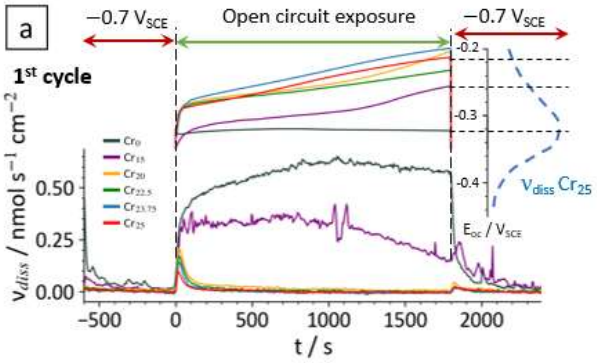

Fig. 6a

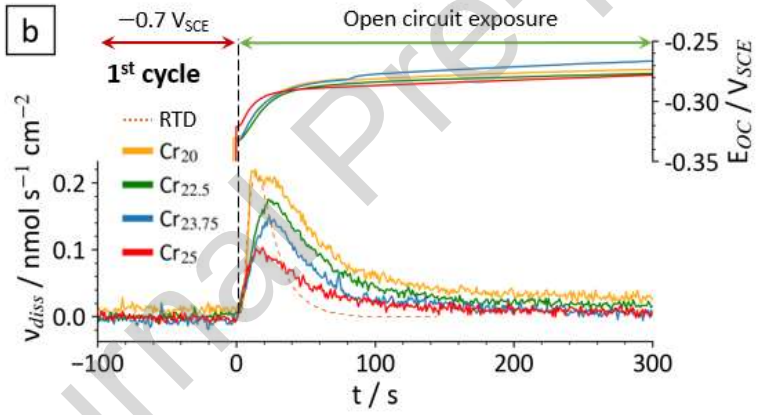

Fig. 6b

Fig. 6 Spontaneous Passivation kinetic profiles. a) Potential and total dissolution curves of $(CoFeNi)_{(100-x)/3}Cr_x$ (x = 0, 15, 20, 22.5, 23.75, 25 at. %) alloy in 0.1 M H_2SO_4 (air bubbled) following cathodic activation (−0.7 V_{SCE}) and OCP. b) An enlarged curve from during the first 300 s. The dashed curve in 6b gives the experimental residence time distribution of the flow cell. Other examples of the spontaneous passivation kinetic profiles are presented in supplementary materials (**Fig. S4 a**). A boxcar averaging (N = 5) was used for the ASEC results to improve the signal-to-noise ratio.

Fig. 7

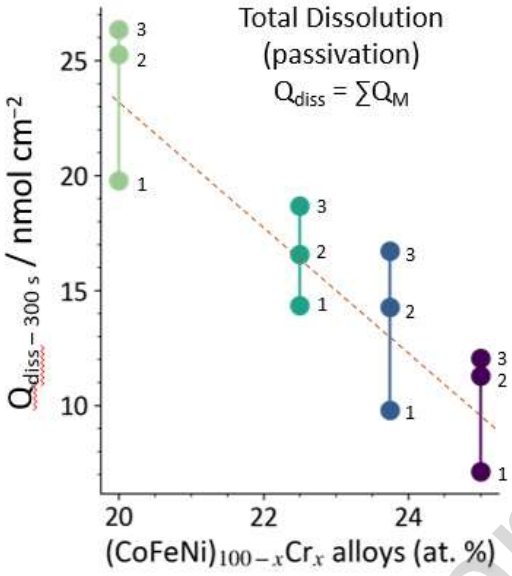

Fig. 7 The total quantity of alloy dissolved ($Q_{diss} = Q_{Co} + Q_{Cr} + Q_{Fe} + Q_{Ni}$) as a function of %Cr for three spontaneous passivation cycles. The points are labeled with the respective cycle number. The total quantity of dissolved species decreases with increasing %Cr and increases with successive active-passive cycles. The accumulative dissolution curves and values are shown in supplementary materials (**Fig. S4b** and **Table S7**).

Fig. 8

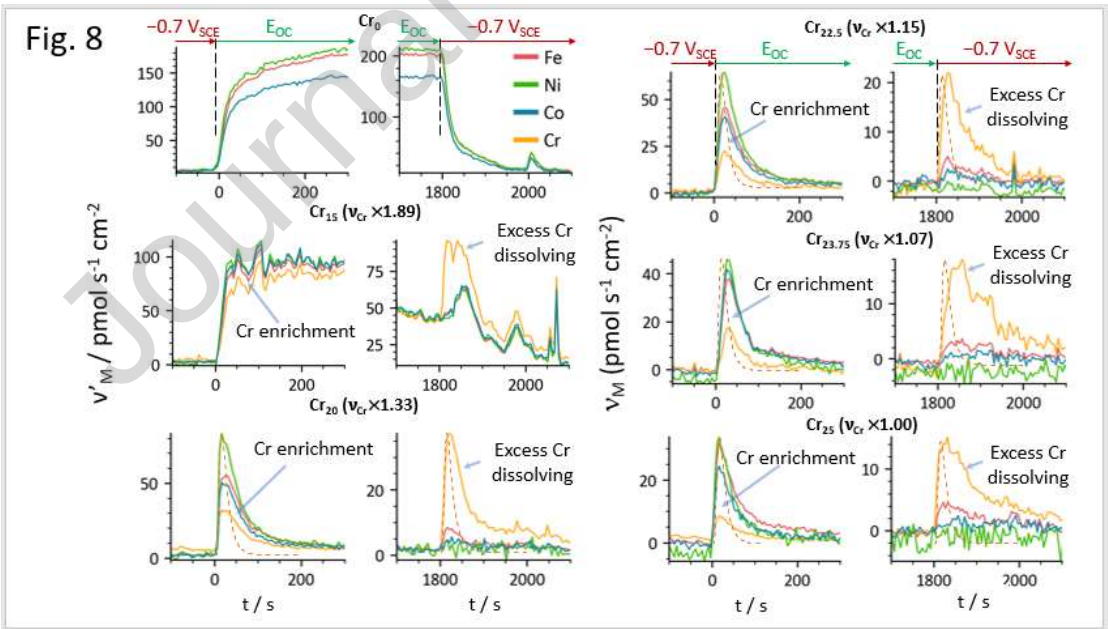

Fig. 8 Elemental dissolution profiles during
first and third columns- spontaneous passivation for the first 300 s;
second and forth columns)- subsequent activation (from 1800 to 2100 s).
Elemental dissolution rates are normalized based on hypothetical congruent Cr dissolution rate (nominal bulk composition) of $(CoFeNi)_{(100-x)/3}Cr_x$ alloys. The dashed

curve gives the experimental residence time distribution of the flow cell. The other cycles are shown in supplementary materials (**Fig. S5 – S9**). A boxcar averaging (N = 5) was used for the ASEC results to improve the signal-to-noise ratio.

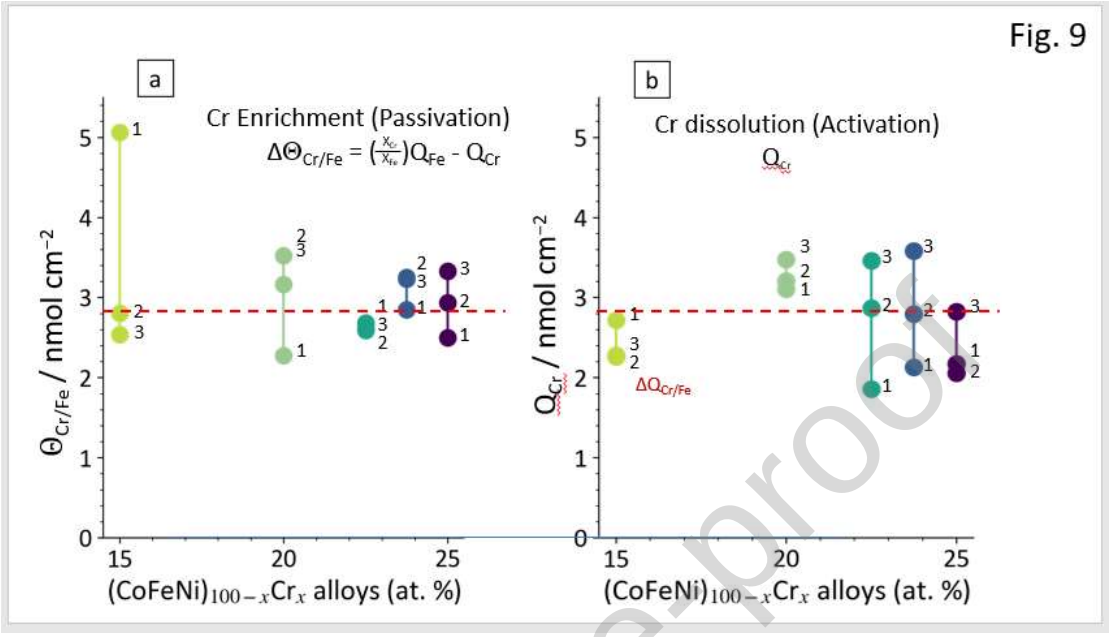

Fig. 9 (a) Cr enrichment during spontaneous passivation; and **(b)** Cr dissolution during cathodic activation as a function of %Cr. The Cr dissolution of Cr_{15} subtracted the Fe dissolution due to the dissolution at end does not reach around 0. Tabulated data are provided in supplementary materials (**Table S8 – S10**).

Fig. 10

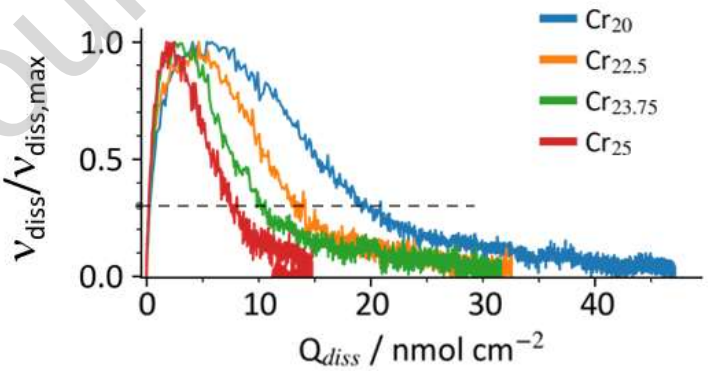

Fig. 10 Relative dissolution rate ($\nu_{diss}/\nu_{diss,\,max}$) as a function of the quantity of alloy dissolved (Q_{diss}) during spontaneous passivation (3rd cycle) of Cr_{20} to Cr_{25} alloys. The dashed line indicates the 30% of the maximum dissolution and the vertical arrows indicate the Q_{diss} at this inhibition level.

Fig. 11

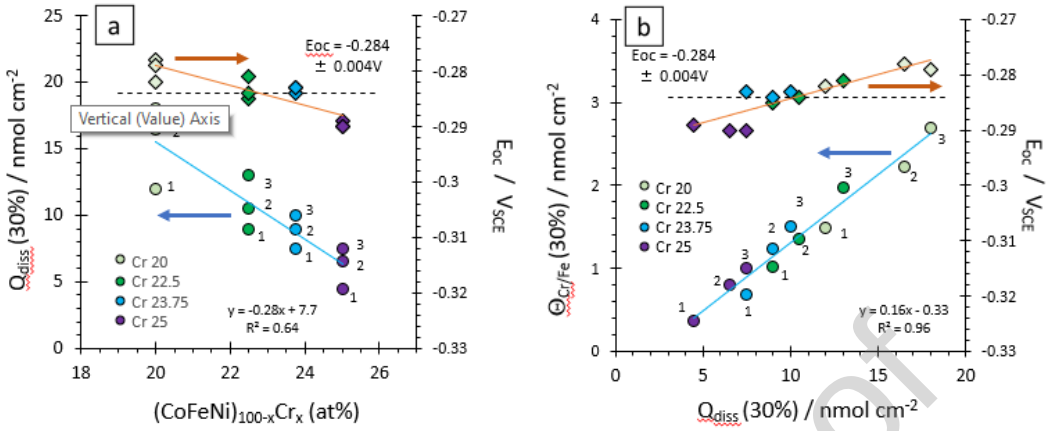

Fig. 11 (a) The quantity of dissolved alloy at the point of 30% reduction of the maximum dissolution rate during spontaneous passivation (Q_{diss} (30%)) (circles) and the corresponding E_{oc} as a function of the %Cr (diamonds)**. (b)** Corresponding Cr enrichment, $\Theta_{Cr/Fe}$ (30%) as a function of Q_{diss} (30%). Three cycles of the spontaneous passivation results and fitting parameters are shown and indicated by the numbering.

Fig. 12

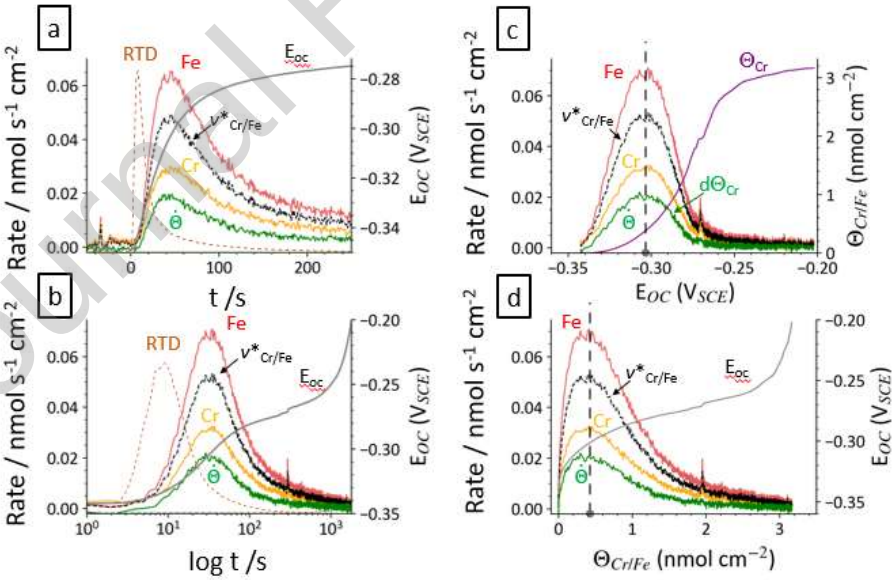

Fig. 12 Relationships between dissolution parameters. Left: a) Initial spontaneous passivation from the end of the last 50 s of activation to the first 250 s of OCP; b) Dissolution profile on a log-time scale showing the OCP, the dissolution rates of Fe and Cr, the hypothetical congruent Cr dissolution rate, and the estimated rate of Cr enrichment. Right: c) The dissolution profiles and Cr enrichment amount (Θ_{Cr}) as a function of E_{OC}; d) The dissolution profiles and E_{OC} as a function of Cr enrichment amount (Θ_{Cr}). The dashed light brown curves in (a) and (c) are the experimental RTD

value. A boxcar averaging (N = 5) was used for the ASEC results to improve the signal-to-noise ratio except the E_{oc} and Θ_{Cr}.

Fig. 13

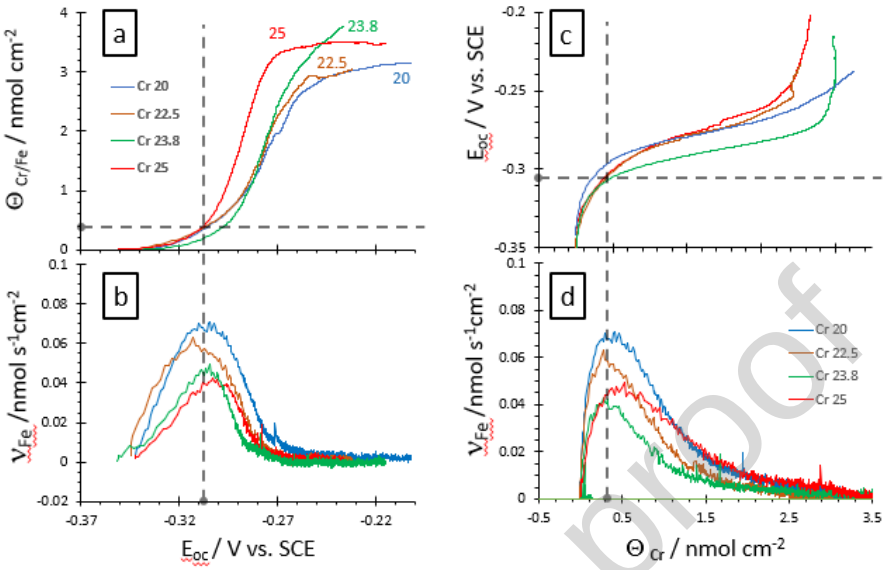

Fig. 13 Relationships between dissolution rate, Θ_C and Eoc. Dissolution rate vs. potential profiles (left) and vs. Cr enrichment (right) for the second cycle of spontaneous passivation for the Cr containing alloys. Shown are the dissolution rates of Fe and Cr, the hypothetical congruent Cr dissolution rate (dashed curve), and the estimated rate of Cr enrichment.

Declaration of interests

☒ The authors declare that they have no known competing financial interests or personal relationships that could have appeared to influence the work reported in this paper.

☐ The authors declare the following financial interests/personal relationships which may be considered as potential competing interests:

CRediT author statement:

Chenyang Xie: Conceptualization, Data curation, Investigation, Methodology, Writing – original draft. **Junsoo Han:** Conceptualization, Writing – review and editing. **Junhui Tang:** Investigation, Resources. **Fan Sun:** Investigation, Resources, Writing – review and editing. **Kevin Ogle:** Conceptualization, Funding acquisition, Methodology, Supervision, Writing – review and editing.

Graphical abstract

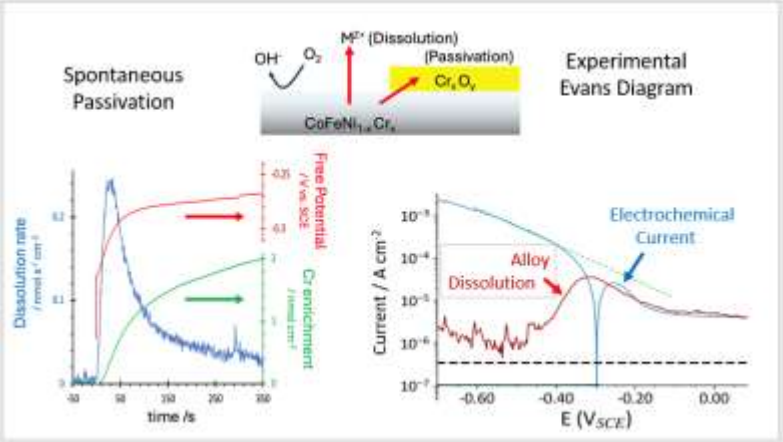

Highlights

- Spontaneous passivation monitored *in situ* by atomic spectroelectrochemistry.
- Passivation determined by critical dissolution rate as compared to the cathodic rate.
- Cr enrichment is the main factor responsible for passivation.
- Passivation correlates with a constant Cr enrichment.
- Stoichiometric relationships between dissolution rate, quantity of dissolved alloy, Cr enrichment, and the open circuit potential are determined.